Nuclear Materials and Energy 12 (2017) 1282–1287

Contents lists available at ScienceDirect

Nuclear Materials and Energy

journal homepage: www.elsevier.com/locate/nme

Isolated nano-tendril bundles on tungsten surfaces exposed to radiofrequency helium plasma

Kevin B. Woller*, Dennis G. Whyte, Graham M. Wright

MIT Plasma Science and Fusion Center MIT, 175 Albany St., Cambridge, MA, USA, 02139

ARTICLE INFO

Article history:
Received 16 July 2016
Revised 18 April 2017
Accepted 27 April 2017
Available online 12 May 2017

Keywords:
Tungsten fuzz
Helium
Nano-tendril
RF sheath

ABSTRACT

The DIONISOS experiment is used to study the impact of RF helium (He) plasma on the surface morphology of tungsten (W) at a frequency of 13.56 MHz. Helium ion energy distributions with a span of 70–75 eV, while still below the sputtering threshold result in nano-tendril bundles (NTBs) and free-standing W whiskers on surfaces at 1020 K. The NTBs are distributed intragranularly with coverage of less than 10% while reaching up to 30 μm normal to the surface for He ion fluence of 7.6×10^{25} m^{-2} and flux density of 10^{22} m^{-2} s^{-1}. Analysis of the NTB interior and sub-surface structure is provided through focused ion beam cross section.

1. Introduction

Tungsten (W) nano-tendrils are likely to form in future fusion energy devices that use W plasma-facing components (PFC). Evidence of the growth of nano-tendrils in the high-power density tokamak experiment Alcator C-MOD further motivates the study of nano-tendril growth [1]. Large areal coverage of W nano-tendrils impacts the plasma-surface interactions [2] and PFC properties [3]. Research is on-going to understand the fundamental mechanisms that drive nano-tendril and fuzz growth. Here, we make a distinction that a nano-tendril is a metal whisker that contains voids filled with helium (He) and fuzz is a large surface area, greater than or equal to the grain size, covered with a porous layer of intertwining nano-tendrils. There are two basic mechanisms for modeling W fuzz growth: (1) pressure driven deformation [4–6] by high pressure He bubbles ($P_{He} \gtrsim 1$ GPa) or (2) surface diffusion [7,8] of ion-induced adatoms (adsorbed atoms) or by viscous flow [9]. Adatoms in the latter group of models are W surface atoms that have been pushed onto the surface either by He bubble growth near the surface or by the He ion bombardment directly. Through measurements we have made of the He concentration during W fuzz growth [10], we know that the He bubbles in the W fuzz layer do not possess the high pressures necessary to deform the surface. For surface diffusion models, the growth environment has been so far too complex to directly observe that adatoms are, in fact, migrating to form such complex nanostructures. Indirect evidence that surface diffusion might be behind surface morphology changes under He plasma irradiation is seen in the nano-ripple patterns that are present before nano-tendril growth, a common feature in epitaxial growth and sputter patterning [11], which are due, in part, to surface diffusion.

While developing in situ Elastic Recoil Detection for our study of the dynamic He concentration in W during He plasma irradiation, a new variant of the nano-tendril surface morphology was discovered, nano-tendril bundles (NTBs) [12]. In this paper, we show that the radiofrequency (RF) sheath is integral to NTB growth. The NTB and single nano-tendril provide additional clues to the growth mechanisms of nano-tendrils in general. Tokamaks use RF wave injection for current drive and heating. The RF waves in the plasma affect the plasma–surface interactions either through sheath rectification [13] or, if the conditions are such that the ions can respond on the RF time scale, by time-modulating the ion energy [14,15]. Thus, like W fuzz, the circumstances that lead to the growth of NTBs may be present in future fusion energy devices, as well.

2. Materials and methods

The samples used were 99.95% pure W disks with a diameter of 25.4 mm and a thickness of 1 mm. The surface to be exposed to the plasma was first mechanically polished and then electropolished in a 4% solution of sodium hydroxide (NaOH) kept at 0 °C in a 1 L stainless steel vessel, which also served as the cathode in the electropolish circuit. The W sample was placed in a PTFE block with the edges of the sample sealed with high vacuum silicone

* Corresponding author.
E-mail address: kbwoller@mit.edu (K.B. Woller).

http://dx.doi.org/10.1016/j.nme.2017.04.016

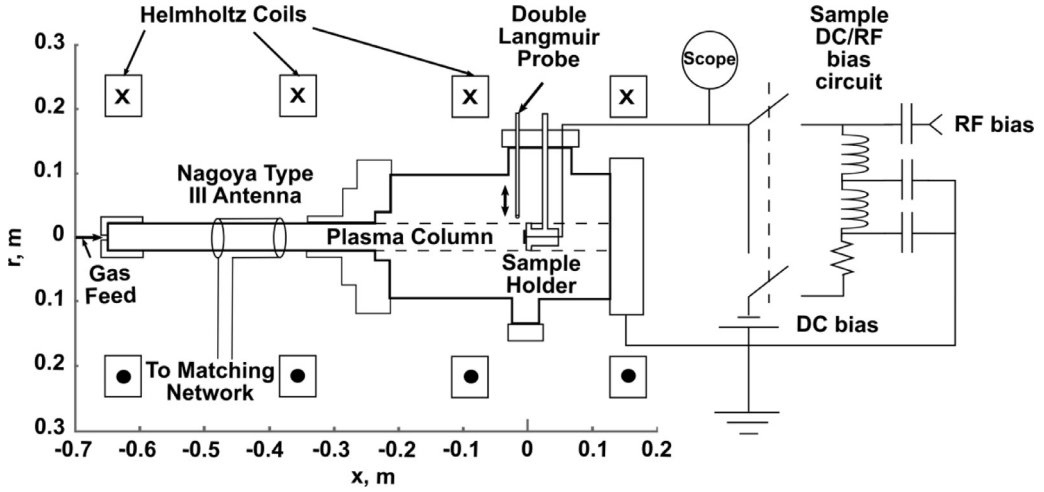

Fig. 1. Schematic of the plasma exposure chamber of the DIONISOS experiment. The DC/RF biasing circuit (not to scale) allows for either DC or RF modulated bias to the target and is monitored with a high frequency probe at the bias feedthrough into the chamber.

grease such that the only exposed area of the anodic side of the electropolish circuit in the NaOH solution was the polished side of the W sample. The best electropolishing conditions were found to be with a voltage of 7 V applied to the W sample and limiting the current to 0.7 A, resulting in a current density of 0.14 A cm^{-2}.

The plasma source used in this work is the 13.56 MHz helicon plasma of the Dynamics of ION Implantation and Sputtering Of Surfaces (DIONISOS) experiment [16]. A cross section schematic of the plasma exposure chamber, along with the major components of the plasma source and sample biasing circuit is shown in Fig. 1. Helicon plasma sources exhibit multiple distinct modes of operation depending on the magnetic field, input power, and neutral gas pressure [17]. For this work, a helicon wave-coupled mode and an inductively-coupled mode were used. The helicon mode was generated with a magnetic field of 0.083 T, input power of 1000 W, and a background He gas pressure of 4 Pa. The inductive mode was generated with a magnetic field of 0.05 T, input power of 700 W, and background He gas pressure of 4 Pa. The flux density and electron temperature radial profile for the two plasma modes, determined with a double Langmuir probe, are shown in Fig. 2.

We analyzed the ion energy distribution function (IEDF) incident on the targets by constructing a single grid-collector retarding field energy analyzer (RFEA) in place of the sample [18]. The grid is a tungsten mesh with a transmission factor of 0.56 mounted on a molybdenum foil with an entrance aperture at the center that is 1 mm by 1 mm. The hole size of the grid, 40 μm, is of the order of 3–4 Debye lengths in these plasmas ($\lambda_D = 10–15\ \mu m$). Since the grid holes are larger than twice the Debye length, degradation of the energy resolution of the RFEA due to curvature of the potential around the grid bars is expected [19]. However, sheath expansion due to the negative bias applied to the grid alleviates this effect. Thus, the grid effectively mimics the conditions present when there is a target mounted on the target holder. The final energy resolution is estimated to be $\Delta E \sim 5$ eV. The space between the grid and the collector was 380 μm, while the ionization mean free path is on the order of 1 cm, so there should be no ionization within the drift space between the grid and the collector. Also, the drift space is narrow enough to avoid space charge effects. To use this grid-collector set up to measure the IEDF incident on a target, we biased the grid with −50 V, swept the voltage on the collector from −100 V to 100 V, and measured the current to the collector simultaneously.

Though simple to implement and compact, the single grid-collector RFEA requires additional considerations of the contribution from secondary electrons to the collector current. The ion current to the collector is the same polarity as secondary electron current leaving the collector. As the collector potential is swept, the current to the collector shows two levels of saturation. The highest level of saturation occurs when the collector potential is lower than the grid bias, as seen in Fig. 3a for the RFEA used to measure the IEDF in the inductive mode plasma. The net current collected saturates when the collector potential is below the grid bias because the secondary electron emission from the collector is lost from the analyzer to the plasma. When the collector potential sweeps above the grid bias, the secondary electrons from the collector are effectively suppressed. A second level of saturation is observed in this potential region where the secondary electrons are suppressed and the collector potential is still below the lowest energy ions, so all of the ion current available is collected. The collector current decreases again once the collector potential is high enough to repel the lowest energy ions.

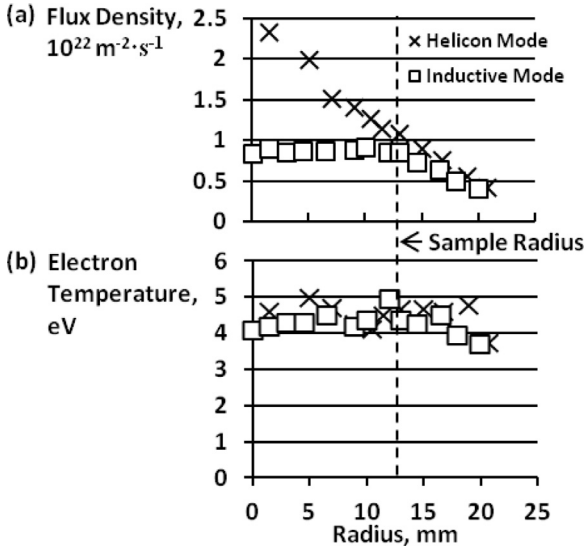

Fig. 2. a) He ion flux density and b) electron temperature radial profiles for the helicon mode (*x*) and the inductive mode (□). Measured with a double Langmuir probe located at x = − 0.01 m in Fig. 1. The sample surface is at x = 0 m.

The current intensity on the collector, shown in Fig. 3b, is the derivative of the measured collector current versus the collector potential, and is proportional to the local IEDF in the plasma after

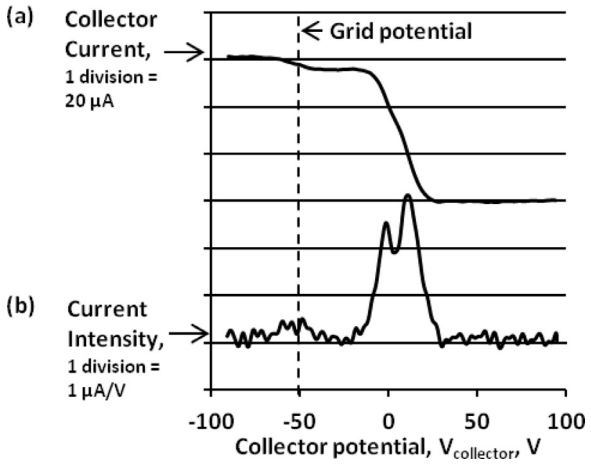

Fig. 3. a) Collector current measured through a grid biased at −50 V as the collector potential is swept from −100 V to 100 V at the center of the inductive mode plasma. b) current intensity, or the derivative of the collector current with respect to the collector potential in a). The current intensity is proportional to the ion energy distribution function passing through the grid.

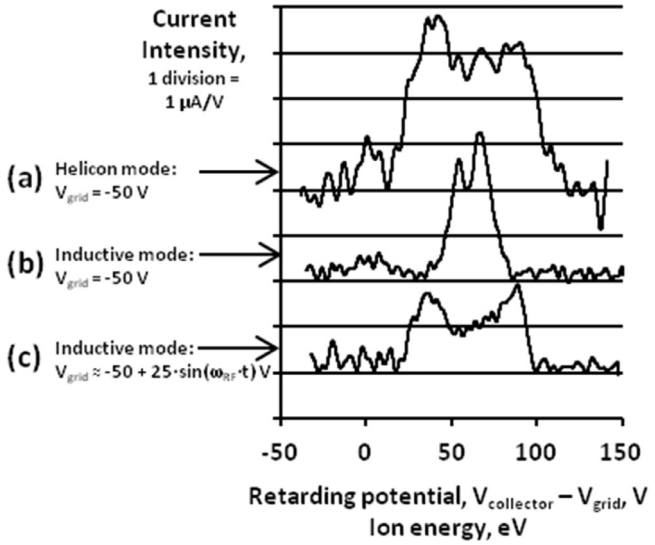

Fig. 4. a) Time-averaged ion energy distribution function (IEDF) measured on axis in the helicon mode through the grid with −50 V DC bias. b) IEDF measured on axis in the inductive mode through the grid with −50 V DC bias. c) IEDF measured on axis for the same inductive mode as in (b) but with a −50 V DC bias modulated with 1 W of RF power at 13.56 MHz resulting in modulation at +/− 25 V. The peak around 0 eV in each measurement is attributable to secondary electron current from the collector.

passing through the sheath and the biased grid. Since the collector potential sweep rate, 0.25 Hz, is much slower than the fluctuations in the plasma or sheath, 13.56 MHz, the current intensity represents the time-averaged IEDF incident on the target at the center of the plasma convolved with the transfer function of the RFEA, which is assumed to be a Gaussian function with a variance of 5 eV and an unknown normalization. However, the shape of the IEDF, not the magnitude, is important here. As can be seen in Fig. 4a, the IEDF at the center of the helicon mode is a broad, bimodal distribution from 25 eV to 100 eV with two dominant peaks in the distribution separated by approximately 50 eV. The bimodal IEDF in the helicon mode is naturally occurring and is the subject of another study that will be reported on elsewhere. In short, the time-averaged IEDF in helicon sources can be broadened due to RF modulation of the plasma potential [20].

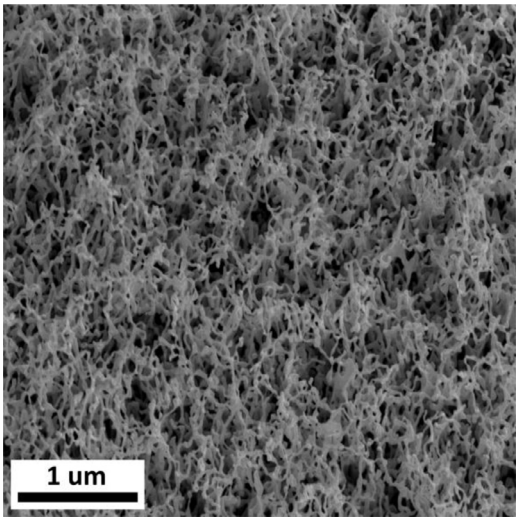

Fig. 5. Scanning electron micrograph of W fuzz grown on a sample at 1020 K in the inductive mode plasma with a DC bias of −50 V for a He fluence of 5.8×10^{25} m^{-2}. The local ion energy distribution is shown in Fig. 4b. The thickness of the W fuzz layer was measured to be 1.5 μm. The viewing angle is 52° from the sample normal.

To isolate the effect of RF broadening or time modulation of the plasma potential in the resulting surface morphology in the helicon mode, we tested the effect of an RF bias on the sample with the plasma in the inductive mode, which has less RF pickup from the antenna and a naturally more narrow IEDF [21]. The IEDF measured at the center of the inductive mode is shown in Fig. 4b. There is little broadening present in the IEDF. To make a baseline comparison to W fuzz growth, we subjected a W sample at 1020 K with a DC bias of −50 V to the inductive mode for a He fluence of 5.8×10^{25} m^{-2} and W fuzz formation was the result, shown in Fig. 5. To impose similar RF broadening in the time-averaged IEDF incident on the sample as in the helicon mode, we constructed a bias tee circuit so that an RF potential could be used to modulate the DC bias to the sample, shown schematically in Fig. 1. The input power from the RF bias supply was selected so that the peak-to-peak value of the modulated sample bias was comparable to the peak-to-peak value of the bimodal IEDF measured in the helicon mode, approximately 50 V peak-to-peak. This required only 1–2 W of RF power. The voltage waveform, from which the peak-to-peak potential was measured, was monitored with a high frequency voltage probe on the bias feedthrough into the plasma chamber. The resulting IEDF measured through the grid with the RF modulated bias in the inductive mode, shown in Fig. 4c, is bimodal with similar FWHM and peak-to-peak potential as the IEDF measured at the center of the helicon mode, Fig. 4a. The exposure conditions are summarized in Table 1.

3. Results

3.1. Ion energy modulation effects

Initially, the NTB structures, shown in Fig. 6a and b, were observed after a W sample with a surface temperature of 1020 K and DC bias of −50 V was exposed to the helicon mode of DIONISOS. The local He fluence at the location where the SEM images were taken (Fig. 6a and b) is estimated to be 7.6×10^{25} m^{-2}. A layer of fuzz with a gradient in layer thickness might be expected due to the gradient in the flux density measured in the helicon mode, Fig. 2a. However, at the center of the sample, which has a broad, bimodal IEDF as shown in Fig. 4a, we found the macroscopic reflectivity of the sample relatively unchanged. Upon closer inspection with a scanning electron microscope (SEM), we discovered the re-

Table 1
Exposure conditions.

		Helicon mode $V_{bias} = -50$ V	Inductive mode $V_{bias} = -50$ V	Inductive mode $V_{bias} = -50 + 25\sin(\omega_{RF} \cdot t)$ V
Input power,	W	1000	700	700
Magnetic field,	T	0.083	0.050	0.050
Fill pressure,	Pa	4	4	4
Peak flux density,	10^{22} m^{-2} s^{-1}	2.5	0.9	0.9
Central exposure fluence,	10^{25} m^{-2}	7.6	5.8	5.8
Electron temperature,	Ev	4.5	4	4
Average ion energy,	eV	63	56	54
IEDF FWHM,	eV	75	24	71

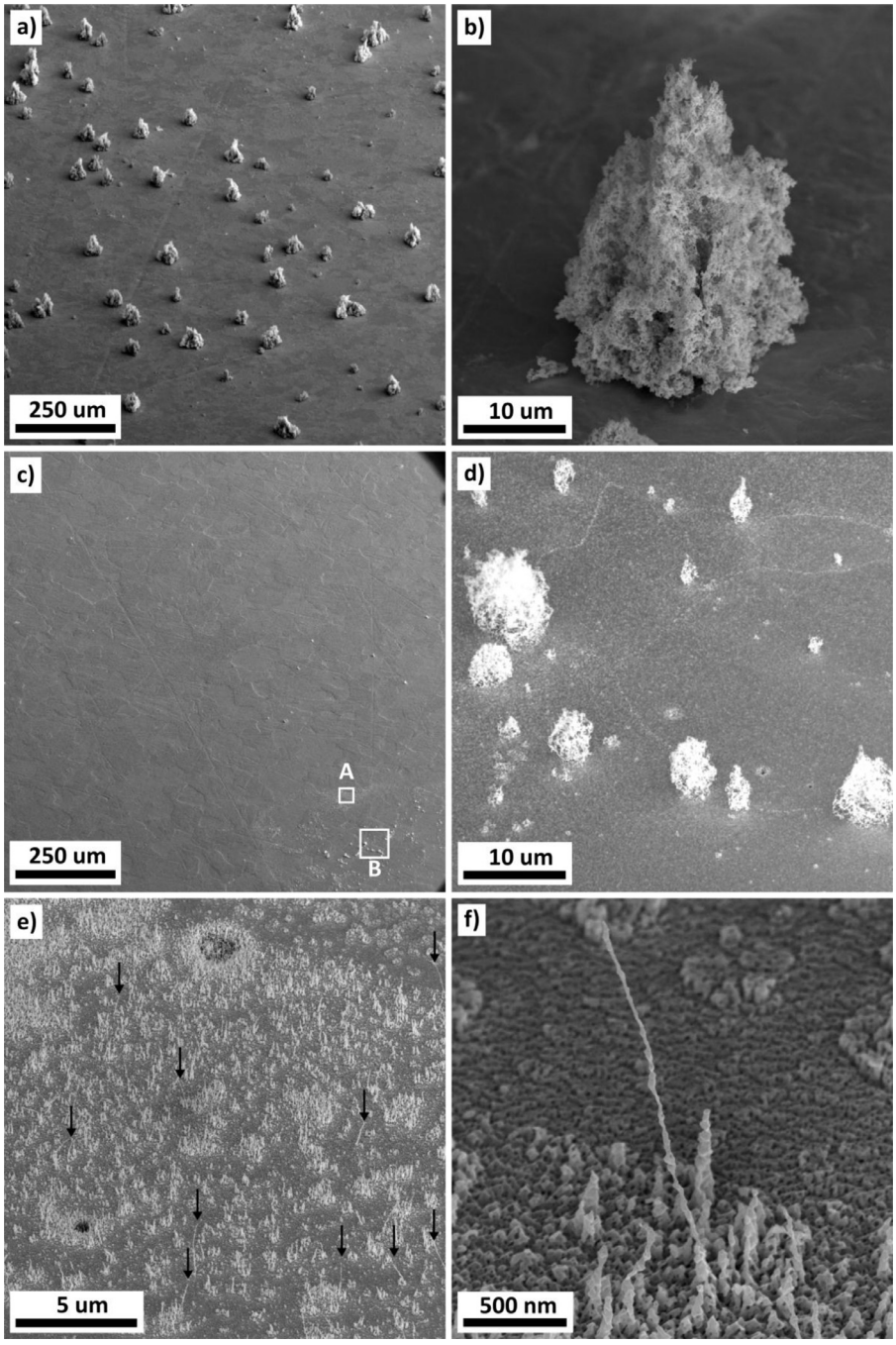

Fig. 6. a) Scanning electron micrograph showing Nano-Tendril Bundle (NTB) growth on a W sample after exposure at 1020 K in the helicon mode plasma with a DC bias of −50 V for a surface averaged He fluence of 7.6×10^{25} m^{-2}. The local He ion flux density of the area in view was 2.5×10^{22} m^{-2} s^{-1}. The local ion energy distribution under these conditions is shown in Fig. 4a. b) micrograph of a NTB from the same sample as shown in a). c) micrograph near the center of a sample exposed with the RF modulated bias in the inductive mode plasma for the same He fluence as the sample in Fig. 5. d) detail of the NTB growth in box labelled B in c). e) detail of the grain in the box labelled A in c) showing multiple single nano-tendrils growing on the grain, some indicated with black arrows. f) detail of a single nano-tendril from the grain in d). all viewing angles are 52° from the sample normal.

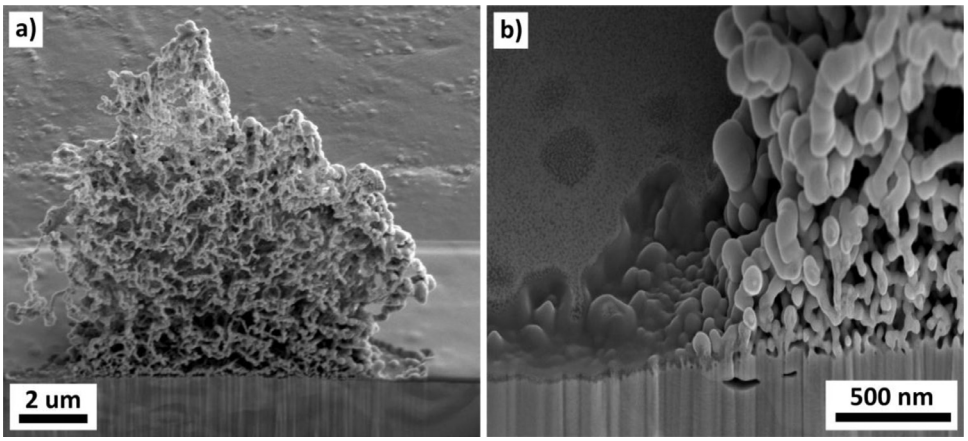

Fig. 7. a) Scanning electron micrograph of a nano-tendril bundle near the center of a sample exposed at 1020 K to a He fluence of 7.6×10^{25} m^{-2} in the helicon mode plasma after coating with platinum and milling with a gallium ion beam showing the cross section of the nano-tendril bundle. b) higher resolution image of a portion of the nano-tendril bundle cross section showing more detail of the difference in the surface morphology between the nano-tendril bundle and the surrounding area, as well as the sub-surface microstructure.

flective area of the sample still had nano-tendril growth, but in the form of NTBs. The area remained mostly reflective due to the low coverage (<10%) of the NTB structures, as seen in Fig. 6a, and the relative smoothness of the surrounding area.

To confirm that the broad, bimodal IEDF is the reason for the NTB growth that forms instead of fuzz using the helicon mode plasma, we applied the RF modulated bias to a W sample at 1020 K and subjected the sample to the inductive mode for the same amount of total collected charge as the W fuzz sample exposed with only a DC bias to the inductive mode, or the equivalent of a He fluence of 5.8×10^{25} m^{-2}. The sample remained macroscopically reflective, except for near the edges of the sample and near the mounting clips. The surface morphology of the outer radii of the sample and under the clip hardware was W fuzz.

Microscopic inspection revealed NTB growth in the reflective area, as seen in Fig. 6d, but the NTBs were smaller than those grown in the higher flux density helicon mode. Also, some grains contained a spread of single nano-tendrils growing 2 μm perpendicular to the surface, shown in Fig. 6e and f. The RF modulation of the ion energy is integral to the transition from W fuzz to NTB growth in our device, but the difference in size between the NTBs from the plasma born RF modulation and the sample bias RF modulation could be due to the difference in flux density in the two exposures. The inductive mode has a flux density at the center a factor of three less than the helicon mode. The growth of W fuzz has been shown to have a flux density dependence, but saturates after a certain flux density level is reached and the saturation that could also be dependent on the ion energy and surface temperature [22]. In the present case, the NTB width and height from the surface also increases with increased flux density. The dependence of the NTB growth on varying the exposure parameters will be shown elsewhere.

The areas of the surface that formed W fuzz in the inductive mode, along the outer edge of the sample and near the clip hardware, experience lower flux density. The ion flux density radial profile shown in Fig. 2a was measured 10 mm from the sample axial location. It is unknown how the clip hardware exactly affects the ion flux density incident on the sample at these locations, but the clips are 3 mm proud of the surrounding sample surface and could shadow the sample at larger radii, which is shown to diminish the flux density in simulations of plasma flux density around non-planar surfaces performed by Kawamura et al. [23]. In their simulations, the flux density is decreased by an order of magnitude, and assuming that the electron temperature is unchanged, this means that the electron density is decreased, as well. The lower plasma density means that the sheath thickness increases in these areas, with the final effect of rectifying the time-modulation we imposed [13,14]. Therefore, the IEDF incident on the sample surfaces at these larger radii is most likely narrow, similar to the IEDF shown in Fig. 4b.

3.2. Nano-Tendril bundle cross section

The NTB structure was analyzed in more detail by milling with a focused-ion beam in the SEM. To protect the fine structure of the NTB, a layer of platinum was deposited over the NTB prior to milling. The NTB after milling is shown in Fig. 7a. A close up of the base of the NTB is shown in Fig. 7b. The nano-tendrils that make up the NTB are very similar in size to the nano-tendrils found in W fuzz. The porosity of the NTB is estimated to be 0.85 from analysis of the image, which is similar to the porosity of W fuzz [24–26].

From the cross section, it is revealed that the interface of the NTB and the bulk is almost level with the surface of the surrounding area, relative to the height of the NTB. Also, there is not a network of voids below the NTB from which the W that composes the NTB could have come. Viewing more closely, in Fig. 7b, one can see that the surface level is lower than the bulk material just below the NTB by 150 nm. Put another way, the NTB seems to be situated atop a pedestal of solid W. The lack of a network of voids below the surface level line and the presence of the solid pedestal indicate that the W that composes the NTB did not come from bulk diffusion from directly beneath the NTB. The W that formed the NTB must have come from the surrounding area.

4. Discussion

There are several possible reasons why the surface morphology is affected by the modulation of the incident ion energy. First, the range of the He ions into the W depends on the ion energy. With ion energies between 25 eV and 100 eV, the He ions penetrate from just one monolayer, or 0.5 nm, to 5 nm. This difference in implantation range is shown by Ito et al. to affect the resulting height of nano-tendril structures given the same total He fluence in semi-two-dimensional (principal directions: one direction parallel to the surface and the other perpendicular to the surface) MD-MC hybrid simulations [27]. The increased implantation range correlated to a decrease in the incubation fluence, or the amount of injected He prior to nano-tendril growth. If the incubation period is shorter for deeper implanted He, then the growth time is increased, resulting

in taller nano-tendril structures for the same amount of total He fluence. In our experiment, the implantation range is modulated in time, which would correspond to the implantation range being modulated, so this effect might result in a time-averaged change to the incubation fluence over the surface, but cannot account for the two-dimensional variation across the surface.

At the temperature of 1020 K under He ion irradiation, the surface develops pores with spacing of approximately 20–30 nm [28,29]. Assuming that the areal density of pores represents the concentration of bubbles below the surface within the W lattice, then the distance between the dominant traps of He in the lattice is also on the order of 20–30 nm. The diffusivity of He in W at 1020 K is approximately 10^{-8} m^2 s^{-1} [30,31]. Thus, the He lifetime when only considering diffusion and accumulation in bubbles is 40 ns, which is close to the RF time period, 74 ns. However, the He flux is continuous, so the effect of ion energy modulation would not have a great impact on the diffusion of He, but might affect the bubble field development through the implantation range, as discussed above. A more detailed evaluation of the nanometer-sized bubbles or voids below and surrounding the NTB structure may provide more evidence of possible growth mechanisms.

Another parameter affected by the incident He ion energy is the adatom yield on the surface. The threshold energy for adatom production exists somewhere above the surface potential energy barrier (~5 eV) [32] and below the threshold energy for sputtering (~100 eV) [33]. Others have shown that the adatom yield is comparable to the sputter yield for incident ion energies above the threshold for sputtering [34,35]. So, for our experiment, with ion energies rapidly changing from 25 eV to 100 eV, the threshold for adatom production would be crossed in each RF time period, effectively pulsing the adatom concentration on the surface. For pulsed laser deposition (PLD) experiments, film growth is affected by the pulse "on" time, the time between pulses, the deposition flux, and the lifetime of the adatoms diffusing that form the film [36]. In our experiment, the adatom lifetime can be estimated from the maximum adatom production rate and the adatom diffusivity. The adatom production rate, Γ_a, is the product of the adatom yield, Y_a, and the incident He ion flux density, Γ. Assuming the adatom yield is approximately 10^{-3} [7], the adatom production rate would be on the order of 10^{19} m^{-2} s^{-1}. This is a very high value, corresponding to 0.5 monolayers of W per second (ML·s^{-1}). By taking the surface temperature in our experiment, 1020 K, the diffusivity of surface self-diffusion can be estimated with the pre-exponential factor $D_0 \sim 10^{-7}$ m^2 s^{-1} and activation energy $E_a = 0.92$ eV [37] to be $D_{1020K} = 2.8 \times 10^{-12}$ m^2 s^{-1}. We assume that the loss of adatoms at the beginning of He ion irradiation is mainly due to recombination with vacancies, which are generated simultaneously with the adatoms. The vacancies are distributed within the first few monolayers of W, but the majority of vacancies are in the original surface layer [35]. If the concentration of vacancies at the surface is approximately equal to the adatom concentration, then the adatom lifetime is estimated as $(\Gamma_a \cdot D_{1020K})^{-1/2}$. This gives an adatom lifetime of approximately 200 μs, but the RF period is 74 ns. This means that the pulse of adatoms during one RF time period would not have enough time to decay until the next pulse of adatoms, approximating a monoenergetic ion irradiation. Preliminary testing of the extent of the frequency range of NTB growth shows that suppression of W fuzz growth is still achieved with a frequency of 20 kHz, which has a period of 50 μs, while keeping all other exposure conditions the same, indicating that NTB growth can be studied at lower frequency.

5. Conclusion

RF broadened ion energy distribution and/or ion energy modulation was shown to affect the resulting surface morphology when He plasma is incident on W at 1020 K. Tungsten fuzz was suppressed, but nano-tendrils were still present. Nano-tendril bundles, essentially islands of nano-tendrils with low coverage (<10%), and single nano-tendrils are observed instead of W fuzz. These new forms of nano-tendril surface morphology provide additional clues for the study of W fuzz growth mechanisms. Ion energy modulation provides a new parameter to study and control the resulting surface morphology.

Acknowledgments

This work is supported by US DOE award DE-SC00-02060 and DE-FC02-99ER54512. This work made use of the MRSEC Shared Experimental Facilities at MIT, supported by the National Science Foundation under award number DMR-08-19762.

References

[1] G.M. Wright, D. Brunner, M.J. Baldwin, R.P. Doerner, B. Labombard, B. Lipschultz, J.L. Terry, D.G. Whyte, Nucl. Fusion 52 (2012) 42003.
[2] S. Takamura, T. Miyamoto, N. Ohno, Nucl. Fusion 52 (2012) 123001.
[3] S. Kajita, S. Takamura, N. Ohno, D. Nishijima, H. Iwakiri, N. Yoshida, Nucl. Fusion 47 (2007) 1358–1366.
[4] A. Lasa, S.K. Tähtinen, K. Nordlund, EPL (Europhys. Lett.) 105 (2014) 25002.
[5] S. Takamura, Y. Uesugi, Appl. Surf. Sci. 356 (2015) 888–897.
[6] A.M. Ito, A. Takayama, Y. Oda, T. Tamura, R. Kobayashi, T. Hattori, S. Ogata, N. Ohno, S. Kajita, M. Yajima, Y. Noiri, Y. Yoshimoto, S. Saito, S. Takamura, T. Murashima, M. Miyamoto, H. Nakamura, Nucl. Fusion 55 (2015) 73013.
[7] Y.V. Martynenko, M.Y. Nagel, Plasma-Surf. Interact 38 (2012) 996–999.
[8] D. Trufanov, E. Marenkov, S. Krasheninnikov, Phys. Procedia 71 (2015) 20–24.
[9] S.I. Krasheninnikov, Phys. Scr. T 145 (2011) 14040.
[10] K.B. Woller, D.G. Whyte, G.M. Wright, J. Nucl. Mater. 463 (2015) 289–293.
[11] W.L. Chan, E. Chason, J. Appl. Phys. (2007) 101.
[12] K.B. Woller, D.G. Whyte, G.M. Wright, in: 2015 IEEE 26th Symp. Fusion Eng, Austin, Texas, IEEE, 2015, pp. 1–6.
[13] R. Ochoukov, D.G. Whyte, D. Brunner, I. Cziegler, B. LaBombard, B. Lipschultz, J. Myra, J. Terry, S. Wukitch, J. Nucl. Mater. 438 (2013) S875–S878.
[14] C. Charles, A.W. Degeling, T.E. Sheridan, J.H. Harris, M.A. Lieberman, R.W. Boswell, Phys. Plasmas 7 (2000) 5232.
[15] T. Panagopoulos, D.J. Economou, J. Appl. Phys. 85 (1999) 3435.
[16] G.M. Wright, H.S. Barnard, L.A. Kesler, E.E. Peterson, P.W. Stahle, R.M. Sullivan, D.G. Whyte, K.B. Woller, Rev. Sci. Instrum. 85 (2014) 23503.
[17] F.F. Chen, Plasma Sources Sci. Technol. 24 (2015) 14001.
[18] K.B. Woller, D.G. Whyte, G.M. Wright, D. Brunner, J. Nucl. Mater. 481 (2016) 111–116.
[19] C. Böhm, J. Perrin, Rev. Sci. Instrum. 64 (1993) 31–44.
[20] J.-H. Kim, H.-Y. Chang, Phys. Plasmas 3 (1996) 1462.
[21] A. Perry, G. Conway, R. Boswell, H. Persing, Phys. Plasmas 9 (2002) 3171.
[22] M.J. Baldwin, R.P. Doerner, D. Nishijima, K. Tokunaga, Y. Ueda, J. Nucl. Mater. (2009) 886–890 390–391.
[23] G. Kawamura, N. Ohno, S. Takamura, Y. Tomita, Nucl. Mater. Energy 0 (2017) 1–5.
[24] M.J. Baldwin, R.P. Doerner, J. Nucl. Mater. 404 (2010) 165–173.
[25] D. Nishijima, M.J. Baldwin, R.P. Doerner, J.H. Yu, J. Nucl. Mater. 415 (2011) S96–S99.
[26] S. Kajita, N. Yoshida, R. Yoshihara, N. Ohno, T. Yokochi, M. Tokitani, S. Takamura, J. Nucl. Mater. 421 (2012) 22–27.
[27] A.M. Ito, A. Takayama, Y. Oda, T. Tamura, R. Kobayashi, T. Hattori, S. Ogata, N. Ohno, S. Kajita, M. Yajima, Y. Noiri, Y. Yoshimoto, S. Saito, S. Takamura, T. Murashima, M. Miyamoto, H. Nakamura, Nucl. Fusion 55 (2015) 73013.
[28] S. Sharafat, A. Takahashi, K. Nagasawa, N. Ghoniem, J. Nucl. Mater. 389 (2009) 203–212.
[29] W. Sakaguchi, S. Kajita, N. Ohno, M. Takagi, H. Kurishita, Plasma Fusion Res. 5 (2010) S1023–S1023.
[30] Y.L. Zhou, J. Wang, Q. Hou, A.H. Deng, J. Nucl. Mater. 446 (2014) 49–55.
[31] X. Shu, P. Tao, X. Li, Y. Yu, Nucl. Instrum. Methods Phys. Res. Sect. B Beam Interact. Mater. Atoms 303 (2013) 84–86.
[32] D. Nishijima, M.. Ye, N. Ohno, S. Takamura, J. Nucl. Mater. (2004) 1029–1033 329–333.
[33] W. Eckstein, Calculated Sputtering, Reflection and Range Values, Garching, Germany, 2002.
[34] T. Michely, C. Teichert, Phys. Rev. B 50 (1994) 11156–11166.
[35] H. Gades, H.M. Urbassek, Phys. Rev. B 50 (1994) 11167–11174.
[36] V. Elofsson, B. Lü, D. Magnfält, E.P. Münger, K. Sarakinos, J. Appl. Phys. 116 (2014) 44302.
[37] W.R. Graham, G. Ehrlich, Thin Solid Films 25 (1975) 85–96.